ADVANCED HEALTHCARE MATERIALS
www.advhealthmat.de
www.MaterialsViews.com

Fluorescence-Tagged Gold Nanoparticles for Rapidly Characterizing the Size-Dependent Biodistribution in Tumor Models

*Leo Y. T. Chou and Warren C. W. Chan**

Nanoparticle vehicles may improve the delivery of contrast agents and therapeutics to diseased tissues, but their rational design is currently impeded by a lack of robust technologies to characterize their in vivo behavior in real-time. This study demonstrates that fluorescent-labeled gold nanoparticles can be optimized for in vivo detection, perform pharmacokinetic analysis of nanoparticle designs, analyze tumor extravasation, and clearance kinetics in tumor-bearing animals. This optical imaging approach is non-invasive and high-throughput. Interestingly, these fluorescent gold nanoparticles can be used for multispectral imaging to compare several nanoparticle designs simultaneously within the same animal and eliminates the host-dependent variabilities across measured data. Together these results describe a novel platform for evaluating the performance of tumor-targeting nanoparticles, and provide new insights for the design of future nanotherapeutics.

1. Introduction

Widespread application of nanomedicine is currently challenged by issues of toxicity and delivery.[1] By virtue of their length scale, nanomaterials administered into a physiological system typically distribute throughout the body and interface with a wide range of compartments and cell types. Interactions of nanomaterials with off-target cells and tissues lower their accumulation at the therapeutic site and effectively diminish their diagnostic sensitivity and therapeutic index. Non-specific sequestration, processing, and redistribution of nanomaterials may also elicit adverse side effects, ranging from inflammation, compromised host defense, to altered gene and protein expression.[2] Moreover, uncertainty over the secondary fates of redistributed nanomaterials has raised concerns of their chronic toxicity. These challenges highlight the need to investigate how the design of nanomaterials affect their in vivo behavior in order to optimize their delivery and improve safety of use.

L. Y. T. Chou, Prof. W. C. W. Chan
Institute of Biomaterials and Biomedical Engineering
Terrence Donnelly Centre for Cellular and Biomolecular Research
Room 450, 160 College Street, Toronto
Ontario, Canada, M5S 3E1
E-mail: warren.chan@utoronto.ca

DOI: 10.1002/adhm.201200084

The in vivo behavior of a nanomaterial is a function of its physical and chemical properties. The size, shape, and surface chemistry of a nanomaterial determine the thermodynamics of its association with proteins, cellular membranes, and tissue structures.[3] The synthetic properties of a nanomaterial (e.g., reactivity, stability, immunogenicity) may evolve over time through these interactions with biological moieties, which ultimately dictates its distribution, bioavailability, and physiological response.[4] In vivo pharmacokinetics of nanomaterials is further complicated by the choice of their dosing regimen and routes of administration, which alter the types of cells and fluids they are exposed to, as well as the sequence and duration of exposure.[5] Given these complexities, the distribution of nanomaterials in vivo must be determined on a case-by-case basis.

Recently, systematic in vivo analysis of nanomaterial pharmacokinetics as it relates to the physico-chemical properties of the nanomaterial have begun to provide a better understanding of nanomaterial non-specificity towards cells and tissues, and a set of metrics for predicting their delivery and toxicity.[3a,6] Emergence of several novel diagnostic and therapeutic strategies underscores the significance of these efforts.[7] However, predictive in vivo structure-activity relationships of nanomaterials do not yet exist, in large because technologies for in vivo pharmacokinetic analysis remain slow and cost prohibitive. Pharmacokinetic and biodistribution data are currently determined using destructive end-point assays (e.g., HPLC, mass spectrometry, ELISA, and radiolabeling),[6a,8] which are time consuming, require a large number of animals, and capture only snapshots of the in vivo transport dynamics. Secondly, despite decades of research there currently exists few nanoparticle platforms that permit systematic and yet robust manipulation of its size, shape, and surface chemistry, which is required to investigate more thoroughly how nanomaterials interface with cells and tissues as a function of their design.

Here we sought to facilitate in vivo evaluation of nanoparticle designs using fluorescent-tagged gold nanoparticles coupled with an optical detection platform. Imaging-guided pharmacokinetic profiling alleviates limitations of end-point assays by allowing non-invasive registration of nanoparticle distribution inside living subjects. Such longitudinal tracking is

advantageous because it reduces animal usage and cost, minimizes inter-animal bias, and preserves data continuity.[9] Compared to other modalities such as magnetic resonance imaging and positron emission tomography, optical imaging has good sensitivity and resolution, is readily accessible, and has available a sizable panel of contrast agents.[10] Optical imaging permits head-to-head comparison of multiple nanoparticle formulations within a single subject by multiplex analysis through spectral unmixing.[10] Its compatibility with molecular biology methods facilitates pharmacokinetic analysis in tandem with functional assays on biological responses such as cell proliferation and protein expression.[11]

Gold nanoparticles (GNPs) are one of the best model nanomaterial for establishing structure-activity relationships because they can be synthesized with well-defined structure and surface chemistry. Methods for the synthesis of gold nanoparticles with a wide range of sizes (i.e., 1–200 nm) and shapes (i.e., spheres, rods, urchins, polyhedrons) are now widely available.[12] More importantly, gold-thiol chemistry provides stoichiometric control over the composition, density, and structural organization of ligands decorating the nanoparticle surface, which has been shown to mediate their interactions with serum proteins, cellular uptake and blood circulation time.[3d,6c,13] However, tracking the uptake and distribution of gold nanoparticles in vivo has generally been laborious and difficult, because the only robust detection methods are either through radiolabeling or destructive elemental analysis.

In this study we systematically optimize fluorescent labeling of gold nanoparticles for in vivo optical analysis. Because it is well known that metals significantly alter the emission of fluorophores near its vicinity in a complex manner,[14] we varied an array of variables (i.e., particle size, ligand length, spectral properties of the dye) and sought to define the synthetic conditions under which fluorescent-labeled gold nanoparticles can be engineered to be sufficiently bright for in vivo detection. We then apply such probes to study the size-dependent kinetics of nanoparticle uptake to solid tumours. In addition, we demonstrate that multispectral imaging could be used to compare the in vivo distribution of multiple nanoparticles simultaneously within a single animal. This study describes a technological platform for the rapid in vivo characterization of nanomaterial designs.

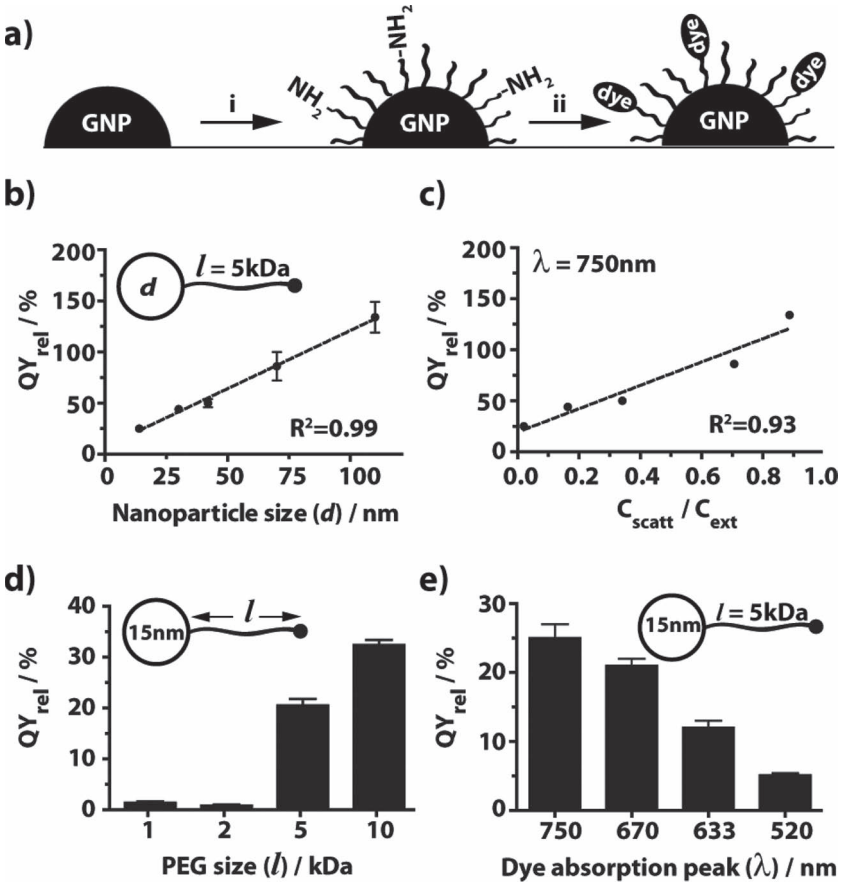

Figure 1. Optimization of fluorescent gold nanoparticle design toward maximal quantum yields. a) Diagram illustrating the synthesis and configuration of fluorescent-tagged gold nanoparticles. **i**: citrate-stabilized gold nanoparticles were incubated at 60 °C for 1 h with a mixture of thiolated-PEG molecules comprising both methoxy- and amine-terminated groups. **ii**: PEGylated nanoparticles were washed and incubated with an excess of NHS-activated fluorophores at room temperature over night. b) The relative quantum yield (QY_{rel}) of the conjugated fluorophore directly correlates with nanoparticle size. Here the dye Alexa Fluor 750 was conjugated to nanoparticles of different sizes separated by PEG 5 kDa as the ligand. c) The same data as in (b) with the data represented as a function of the scattering-to-extinction ratio of the nanoparticles derived from Mie theory. d) The quantum yield of a fluorophore strongly depends on its distance from the metal surface. The model fluorophore Alexa Fluor 750 was conjugated to a 15 nm gold nanoparticle using PEGs of molecular weights 1, 2, 5, 10 kDa. Fluorescence was strongly quenched for PEG lengths below 5 kDa and progressively recovered thereafter. e) Spectral separation between the absorbance peak of the nanoparticle and the dyes impacts the quantum yield of the fluorophores. In general, the quantum yields of the fluorophore increases with the red-shifted spectral separation between the absorbance peak of the nanoparticle and the dye. Values represent mean ± SD (n = 3).

2. Results and Discussion

2.1. Synthesis and Optimization of Fluorescent-Labeled Metal Nanoparticles

We synthesized GNPs varying in size from 15, 30, 45, 75, to 100 nm using previously published techniques,[12c,15] and grafted them with a mixture of thiolated poly(ethylene glycol) (PEG) molecules that contain either methoxy- or amine-terminated functional groups (**Figure 1**a). We quantified the total ligand density grafted on the particle surface using a thiol-depletion assay (see SI), and controlled the number of amines on the particle surface by varying the stoichiometry of the two PEG molecules in the reaction. We chose PEG as the coating ligand because it is currently the most effective polymer for stabilizing nanoparticles in vivo and for delaying

their rate of non-specific uptake by cells of the reticuloendothelial system.[16] In this study we varied the PEG molecular weight from 1, 2, 5, to 10 kDa in order to study the effect of ligand length on the resulting particle fluorescence. Because these ligands can be further conjugated with a variety of molecules, the results from this study serve as a basis for constructing more complex nanoparticle designs for in vivo detection.

To render PEGylated nanoparticles fluorescent, we conjugated them with a 5x molar excess of succinimidyl fluorophores per amine. Covalent attachment of the fluorophores to the GNPs was confirmed with agarose gel electrophoresis (Figure S1 of the Supporting Information (SI)). We further quantified the conjugation efficiency using a fluorescence depletion assay (see SI), which demonstrated near stochiometric conjugation of all available amines on the particle surface with the fluorophores given our synthetic conditions (Figure S2 of the SI). After synthesis, the core and hydrodynamic sizes of the particles were characterized by transmission electron microscopy (Figure S3 of the SI) and dynamic light scattering (Figure S4 of the SI), respectively.

We assessed the impact of metal-fluorophore interactions on the intensity of a fluorescent molecule by measuring its relative quantum yield (QY_{rel})–defined as the ratio of the fluorescence intensity of the dye when conjugated to the particle surface divided by its fluorescence intensity as a free dye:

$$QY_{rel} = \frac{PL_{dye\ on\ particle}}{PL_{free\ dye}} \times 100\%$$

Here we compared four spectrally distinct fluorescent molecules, including Cyto633, Alexa Fluor 750, and two long-stokes shift dyes Cyto522 and X-Sight 670 (see Figure S5 of the SI for the absorbance and emission spectra of these dyes). These dyes were chosen because they emit in the near-infrared wavelegnths, a spectral region with minimal tissue absorbance and scattering, and therefore optimal optical detection sensitivty.[17] Starting with Alexa Fluor 750, we found that its relative fluorescence intensity directly correlated with the size of the nanoparticles (Figure 1b); whereas QY_{rel} of the Alexa Fluor 750 dye was as low as 20% (i.e., quenched) when it is conjugated to the surface of a 15 nm nanoparticle and 134% on the largest nanoparticle (d = 100 nm) tested. This is consistent with theoretical predictions[18] and experimental findings[19] that particles with larger scattering cross-sections (i.e., size) lead to higher QY_{rel}. Indeed, we found that QY_{rel} correlated linearly with the scattering-to-extinction ratios of the corresponding nanoparticles calculated at the absorption peak of the dye (i.e., C_{scatt}/C_{ext} of the nanoparticles at 750 nm, Figure 1c), providing experimental evidence that the optical properties of the nanoparticles can be used to predict the QY_{rel} of fluorescent molecules attached to the GNP surface within the range of sizes tested (see Table S1 for the values of the scattering and extinction coefficients used).

The emission rate of a fluorophore also varies as a function of its distance from the metal surface due to two competing processes: 1) influence in the excitation rate of the molecule due to field enhancements near the metal surface and 2) alterations in its quantum yield due to the balance of radiative and nonradiative energy transfer pathways near the metal.[14a,20] It has been shown previously that the fluorescence of a dye remains quenched for a given range of particle sizes (i.e., d = 2–60 nm) when placed at very short separation distances (i.e., 1–2 nm) from the metal surface due to both an increase in non-radiative energy transfer and a decrease in radiative decay rates.[14d] Consequently, fluorescence quenching that we have observed on small GNPs may be reduced by increasing the distance between the fluorophore and the metal. The use of PEG 1 kDa or 2 kDa as linkers resulted in near complete quenching of Alexa Fluor 750 on a 15 nm GNP and PEG lengths beyond 5 kDa was sufficient for fluorescence recovery (Figure 1d). Dynamic light scattering measurements indicated that a fully extended PEG 5 kDa brush layer adds a hydrodynamic radius of approximately 15 nm to a 15 nm particle surface, suggesting that this distance was required for substantial fluorescence recovery.

To investigate the spectral dependence of GNP-fluorophore interactions, we measured the relative quantum yields of the four dyes conjugated to a 15 nm GNP. The extent of quenching was inversely related to the red-shifted spectral separation between the absorbance peak of the nanoparticle and the fluorophore. For example, on a 15 nm GNP with a surface plasmon peak at ~518 nm, we measured a QY_{rel} of 12% for the fluorophore Cyto633 (ex/em: 637/657 nm) compared to 25% for the longer wavelength emitting Alexa Fluor 750 (ex/em: 753/782 nm) (Figure 1e). In addition, we compared Cyto633 to Cyto520 (ex/em: 520/700 nm), a long Stokes-shift dye with relatively longer emission but shorter excitation maximum (see Figure S5 for the spectra). Interestingly, Figure 1e shows that Cyto633 was more than twice as bright as Cyto520 (12% vs. 5%, respectively), suggesting that maximizing the spectral separation between the absorbance peak of the nanoparticle with both the excitation *and* the emission frequency of the dye are important to reduce fluorescence quenching. Comparing Alexa Fluor 750 with Kodak X-Sight 670 (ex/em: 669/755 nm)–another long Stokes-shift dye–further confirms this observation (Figure 1e).

These results suggest three principles for controlling the fluorescence of dye-labeled GNPs within the size range we tested: 1) the nature of metal-dye interactions (e.g., quenching or enhancement) due to field enhancements near a GNP can be approximated by its scattering-to-extinction ratio, 2) GNP-dye distance must be far enough to promote radiative decay rates and reduce nonradiative energy transfer pathways, and 3) the strength of these interactions depend on the spectral overlap between the GNP and the fluorescent dye.

2.2. Pharmacokinetics Analysis Using Fluorescent Gold Nanoparticles

An application of fluorescent-GNPs of primary concern to us is their capability as in vivo probes for investigating the design-dependent pharmacokinetics and tumour-targeting behaviour of nanomaterials. For this purpose we sought to maximize the density of PEG (ρ_{peg}) on the GNPs, since increasing PEG density has been reported to improve the tumour accumulation efficiency of nanomaterials by increasing their circulation time in blood,[21] and would also maximize probe brightness by increasing the number of binding sites available for dye attachment. From this rationale we mixed GNPs with an excess of thiolated PEG (i.e., 10 PEGs/nm^2) and partially dehydrated PEG to minimize PEG-PEG steric hindrance by performing the grafting reaction at an

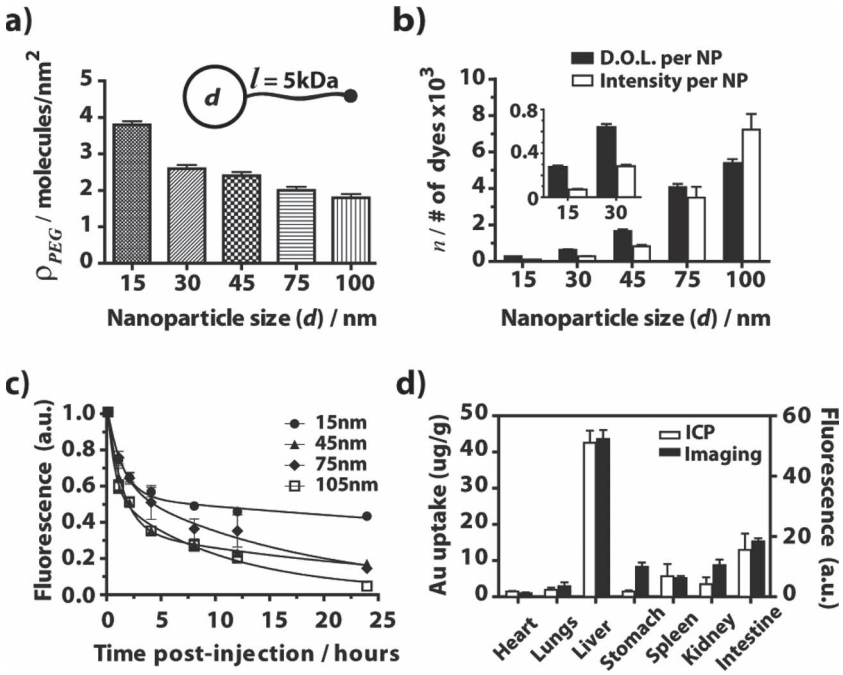

Figure 2. In vivo detection and validation of optical imaging-based pharmacokinetic assessment. a) maximal grafting density of PEG 5 kDa on the nanoparticles as a function of particle size (n = 3). b)The degree-of-labeling (D.O.L.) of fluorophores as a function of nanoparticle size and the quantum yield normalized brightness per nanoparticle expressed as the number of free dye equivalent. Numbers are shown for Alexa Fluor 750 conjugated to the gold nanoparticles via PEG 5 kDa (n = 3). c) Systemic fluorescence intensity as a function of time for nanoparticles of various sizes. Curves are generated by performing image analysis on mice injected with fluorescent-labeled gold nanoparticles over various time points, and fitting the data to a 2-compartment physiological model (n = 3). d) Gold nanoparticle content in organs harvested from mice 24 h after being injected with 15 nm fluorescent-tagged gold nanoparticles. Gold content is measured with both ICP-AES and fluorescence imaging to validate that imaging can provide semi-quantitative assessment of nanoparticle biodistribution ex vivo (n = 4). Values represent mean±SD.

elevated temperature (i.e., 60 °C).[22] These measures resulted in PEG densities ranging from 1.8 ± 0.2 to 3.8 ± 0.3 molecules/nm^2 depending on particle size (**Figure 2**a), which translated to approximately 270 to 5300 fluorophores per particle (Figure S6 of the SI). Using the fluorescence assay we have developed, we measured the QY_{rel} normalized brightness of the nanoparticles, expressed in number of free dye equivalents (n) (Figure 2b and summarized in Table S2 of the SI). Using Alexa Fluor 750 as the dye for conjugation, a single 15 nm GNP had an intensity equal to 70 ± 10 dyes, whereas a 100 nm GNP corresponded to 7100 ± 900 dyes. Theser densely PEGylated fluorescent GNPs exhibited high stability in serum; fluorescent-labeled PEG enabled us to quantify their desorption kinetics from the particle surface following incubation in serum. After 24h incubation in serum at 37 °C, desorption accounted for only 6 to 8% of the total PEG molecules grafted on the nanoparticle surface for all particle sizes examined (Figure S2 of the SI).

We then tested whether fluorecent-labeled GNPs can be detected in vivo and whether their pharmacokinetic behaviors can be assessed using fluorescence imaging. Blood circulation time is a key parameter for effective accumulation of nanoparticles into the tumor.[6a] To assess whether blood pharmacokinetics (PK) can be measured quickly and non-invasively using our platform, CD1 nude mice were administered single intravenous (i.v.) injections of nanoparticles and imaged using a Kodak In Vivo Imaging System at selected time points over a 24h period. Graphs were generated by region-of-interest (ROI) image analysis, from which we derived the elimination blood half-lives ($t_{1/2,\beta}$) of the nanomaterials by fitting to a two-compartment model (Figure 2c; see SI for a description of the ROI-analysis and the pharmacokinetic model used). For all particle sizes, the two-compartment model fitted the data accurately, with r^2 = 0.91 to 0.98. Here we found that particle half-life in circulation improved with decreasing particle size for a given length of PEG as the ligand. Half-life was ~4.4 times greater in 15 nm particles coated with PEG 5 kDa ($t_{1/2}$ = 31.9 h, n = 3) compared to 100 nm particles ($t_{1/2}$ = 7.3 h, n = 3) with the same ligand. These trends are consistent with published findings determined using *ex vivo* techniques.[6c,23] To further validate fluorescence measurements in real biological tissues, we injected a single bolus of Alexa Fluor 750-labeled 15 nm gold nanoparticles stabilized with PEG 5 kDa into CD1 mice and harvested organs 24h post-injection. We measured the biodistribution of nanoparticles by *ex vivo* fluorescence imaging, and correlated the measurements to gold content in the organs by using inductively coupled plasma atomic emission spectroscopy (ICP-AES). Here we found consistent correlation between the two methodologies (Figure 2d, n = 4). Together, these results demonstrate that our fluorescence imaging system could provide rapid and semi-quantitative assessment of nanoparticle distribution in biological samples.

2.3. Image-Guided Analysis of Nanoparticle-Size Dependent Tumor Accumulation Dynamics

We applied fluorescent-labeled gold nanoparticles to investigate the effect of particle size on tumor accumulation dynamics over a 24 h period. Fluorescent-tagged gold nanoparticles of different sizes were systemically injected into xenograft tumor-bearing mice, and whole-body fluorescence was sampled at 0, 1, 2, 4, 8, 12, 24 hours post-injection (n = 4 for each particle size). Accumulation of nanoparticles in the tumor was assessed using region-of-interest analysis (see SI). Here we found quantifiable differences in tumor accumulation dynamics across particle sizes (**Figure 3**a–d); whereas the 15 nm particle design achieved its highest tumor accumulation at 24h post-injection (Figure 3a), maximal uptake was observed at 8 h for the 75 nm and 100 nm gold nanoparticle, and at 4 h for the 45 nm nanoparticle (Figure 3b-c). Retention was also particle-size dependent: at 24 hours post-injection, the 15 nm nanoparticle achieved its maximal signal in the tumor. On the other hand, the 45 nm

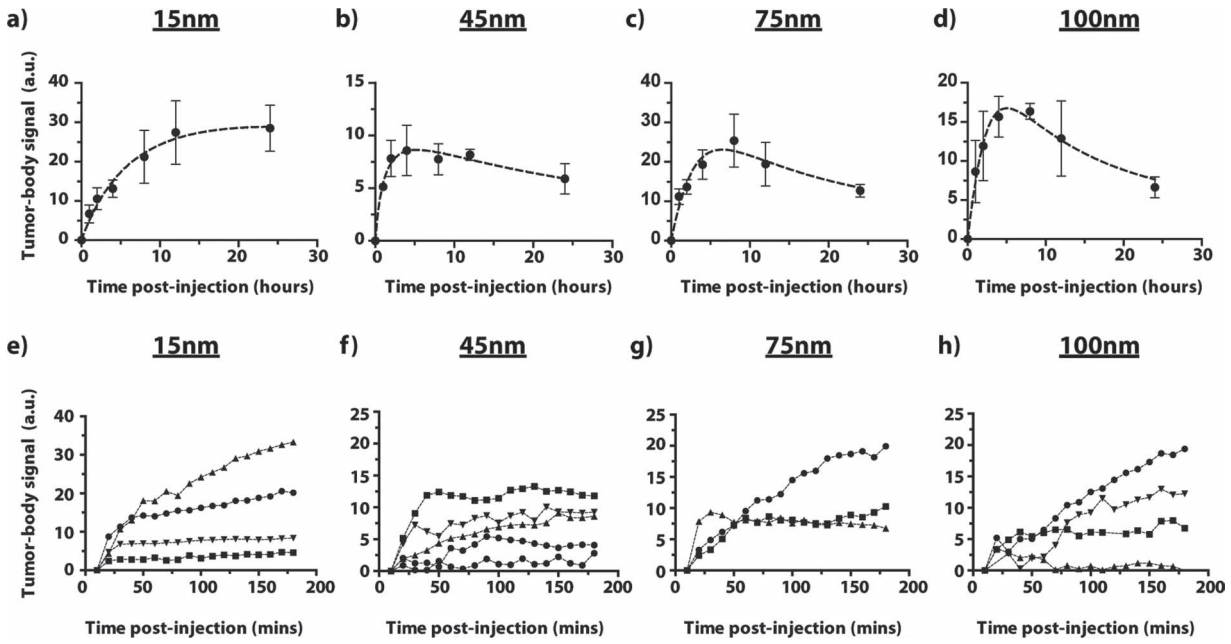

Figure 3. Assessment of tumor targeting dynamics of passively targeted gold nanoparticles by fluorescence imaging. a-d) Tumor accumulation as a function of time for nanoparticles of various sizes. Curves are generated by image analysis of mice injected with fluorescent-labeled nanoparticles over multiple time points. Values represent mean±SD (n = 3-5 for each group of nanoparticle sizes). e-h) Real-time monitoring of tumor accumulation rates for nanoparticles of various sizes. Mice injected with fluorescent-tagged gold nanoparticles were immediately anesthetized and imaged continuously for 180 min to probe the early tumor accumulation kinetics of nanoparticles in real-time. Each curve represents one animal.

particle retained about 70% of its maximal signal within the tumor, while that of 50% and 41% remained for the 75 nm and 100 nm particles, respectively (Figure 3b–d). Differences in the pharmacokinetics, extravasation, and intratumoral permeation of nanoparticles as a function of their sizes[24] could explain such differences in gross accumulation and retention.

We also asked whether particle size could impact its rate of entry (i.e., K_{in}) into the tumor at earlier times post-injection (i.e., 3 hours), when extravasation from the blood vessels into the tumor interstitium is minimally limited by clearance of the injected dose from circulation. To assess this in real-time, CD1 mice bearing unilateral MDA-MB-435 human carcinoma xenografts in the hind flank were administered single i.v. injections of fluorescent gold nanoparticles, and then imaged continuously for 180 minutes at 10-min capture intervals. Region-of-interest analysis revealed that the rate of particle accumulation in the tumor compartment occurred non-linearly as reflected by the non-linear rise in the fluorescence intensity curves in the tumor relative to the contralateral flank over time (Figure 3e–h). In most cases, the increase in fluorescence was biphasic, starting with a rapid rise followed by a slow, gradual increase. The biphasic nature of curves may reflect the distribution and extravasation of nanoparticles into the tumor, or it may reflect the two-phase nature of transport in the tumors.[25] However, the slopes of the two phases were highly variable both within and across particle sizes without any discernible trends.

We hypothesized that tumor heterogeneity may contribute to the high variability in the observed rates of particle accumulation. To investigate this, we grouped tumors with respectively low or high rates of uptake, and analyzed their morphologies by histology. Four serial sections from each tumor were sampled and separately stained with haematoxylin and eosin (H&E) for structural morphology, CD31 expression for microvasculature, Masson's trichrome for extracellular matrix, and silver staining for nanoparticle localization. Representative images of tumor histologies are shown in **Figure 4**a-b. Examining the staining features suggest that nanoparticles co-localized with very specific tissue morphologies. Areas of the tumor containing cells surrounding collapsed vessels (Figure 4a, see arrow in the CD31 panel) and fibrotic areas with a dense patch of extracellular matrix had little nanoparticle staining (Figure 4a). Tumors characterized by high cellular density also showed little nanoparticle staining (Figure S7 of the SI). These results are consistent with past findings that uncontrolled proliferation of cells within tumors can restrict molecular transport by collapsing functional blood vessels and reducing interstital space.[26] Deposition of dense extracellular matrix within the interstitum further impedes transport of molecules as a function of their size. In contrast, areas with reduced cellular density, open blood vessels, and low levels of extracellular matrix showed intense staining for nanoparticle content (Figure 4b). Previous work using magnetic resonance imaging has shown that the apparent diffusion coefficient is significantly higher in such regions,[27] consistent with our data from histology and fluorescence imaging. Several other studies have shown that necrotic regions within the tumor maybe conducive to interstitial diffusive transport due to reduced cellular density.[28] The quantitative impact of tumor morphology and structural heterogeneity on nanoparticle delivery suggests that a multiplexing strategy

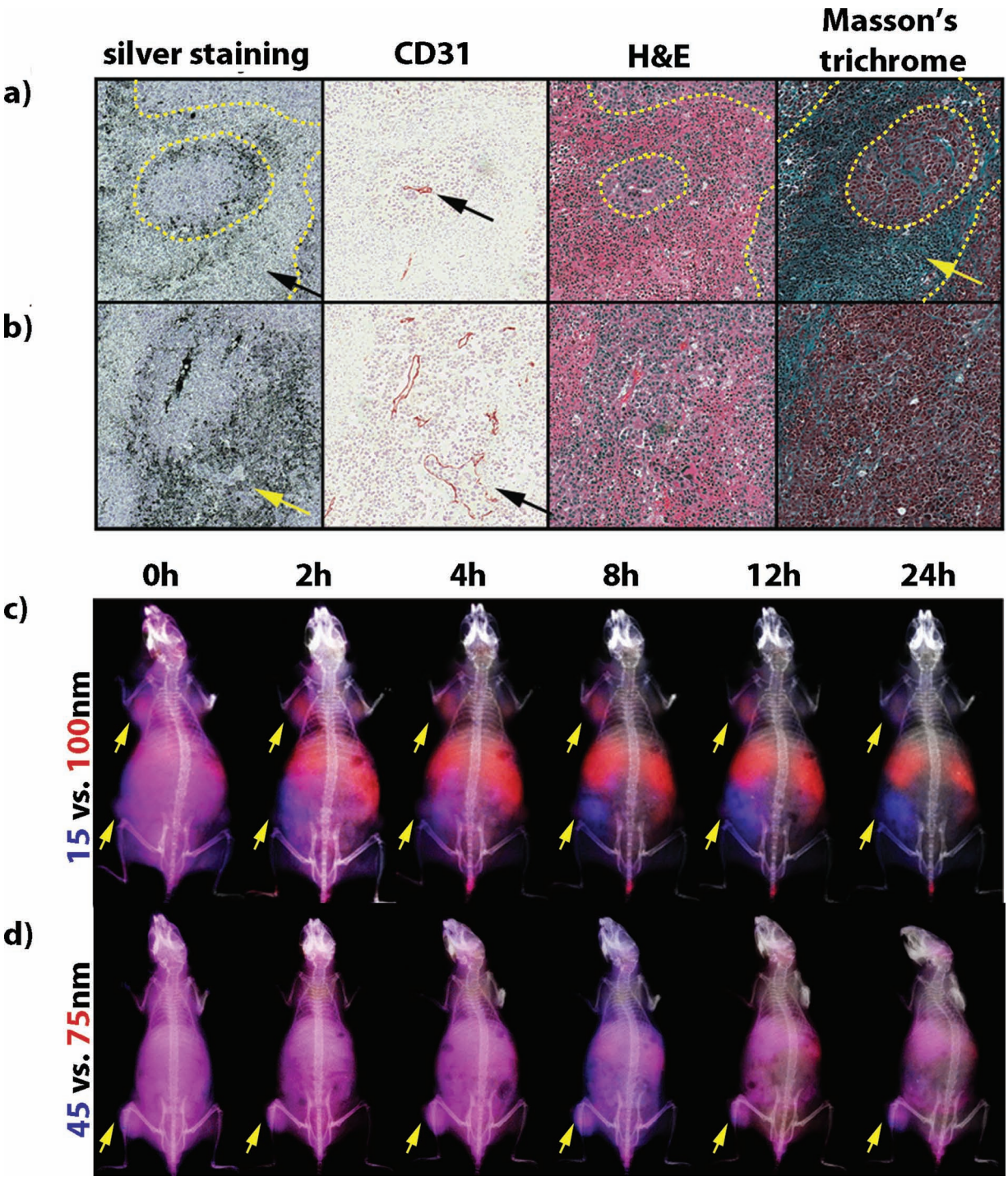

Figure 4. Impact of tumor morpholgy on nanoparticle accumulation assessed by histology and multicolor imaging. a-b) Histological sections of tumors from samples imaged in Figure 3e-h. Serial sections of the tumors were stained with silver for gold nanoparticle content, CD31 for blood vessels, H&E for structural morphology, and Masson's Trichrome for extracellular matrix. a) Little particle staining (black arrow in the silver staining panel) was observed in areas of tissues containing collapsed blood vessels (black arrow in the CD31 panel) and dense patches of extracellular matrix (yellow arrow and dashed outlines in the Masson's Trichrome panel). b) Intense nanoparticle staining was observed in tissue areas with leaky vessels (black arrows in the CD31 panel), reduced cellular density (see the H&E panel), and low extracellular matrix content (see Masson's Trichrome panel). c-d) Appropriately engineered fluorescent-tagged gold nanoparticles enable multicolor in vivo imaging. c) Spectrally unmixed fluorescence images of mice bearing multiple MDA-MB-435 tumors (yellow arrows) injected simultaneously with both 15 nm and 100 nm gold nanoparticless; particles were coated with PEG 5 kDa, and fluorescently labelled with Kodak X-Sight 670 and Alexa Fluor 750, respectively. d) Spectrally unmixed fluorescence images of tumor-bearing mice (yellow arrows denote location of tumor) co-injected with 45 nm and 75 nm fluorescent-tagged gold nanoparticles. These images demonstrate that the extent and dynamics of tumor accumulation varies as a function of both particle and tumor pathobiology (i.e., size and location on the animal), and highlights the potential utility of multiplexing for evaluating the performance of tumor targeted nanoparticles.

is required to analyze how the physico-chemical properties of a nanomaterial affects their pharmacokinetics.

2.4. Multispectral Imaging Using Fluorescent-Labeled Gold Nanoparticles

Several in vivo factors (e.g., animal size and physical state, and tumor pathophysiology) can influence nanoparticle pharmacokinetics and tumor accumulation, producing large variability in the data even at relatively large sample sizes. To eliminate these host-dependent variables, we asked whether multiple nanoparticle formulations could be tracked, and therefore directly compared, simultaneously within a single animal using our optical detection platform.

The Kodak In Vivo Imaging System is capable of performing multichannel measurements by unmixing multispectral image stacks against pre-modeled absorption profiles, which serve as optical signatures for each channel. To maximize signature distinction without loss in temporal resolution, we selected two fluorophores with minimal spectral overlap in their absorption profiles but similar emission wavelength (Alexa Fluor 750 and Kodak X-Sight 670, spectral profiles shown in Figure S5 of the SI). This allowed us to perform multispectral imaging by using a common stack of excitation filters (e.g., from 520 to 730 nm), all captured with a single emission filter (e.g., 790 nm). To test this, each fluorophore was conjugated to a set of nanoparticles, separately injected intramuscularly into the thighs of CD1 mice, followed by imaging using the intended protocol. Using the imaging software, we modeled the in vivo spectral profile of each particle set by fitting Gaussians to the multispectral images, establishing three independent channels, one for each particle set and a third one for the autofluorescence of the skin.

To test the established models for multispectral imaging, CD1 mouse bearing two tumors was co-injected with optically encoded 100 nm and 15 nm particles both stabilized with PEG 5 kDa (Figure 4c). Imaging stacks were sampled over 24 hours and spectrally unmixed using the model. An x-ray image was also taken at each time point for anatomical co-registration. Consistent with single color imaging, we found strongly size-dependent in vivo distribution, including faster liver sequestration of 100 nm particle. More importantly, we observed highly heterogeneous uptake and retention dynamics across the two tumors (yellow arrows, Figure 4c) both within and across each particle design. This supports the need for direct comparison as otherwise the heterogeneity may be averaged as error if particles are compared using two different animals. Examining the tumor located below the left foreleg of the animal, we observed high size-dependency in tumor accumulation dynamics; the larger particle (i.e., red) achieved maximum signal between 4-8 h post-injection followed by gradual decrease up to 24 h, where as the signal of the smaller particle (i.e., blue) steadily increased towards 24 h. These results are consistent with that obtained from single-color imaging for the same nanoparticle sizes (Figure 3a and 3d). Repeating the experiment using 45 nm versus 75 nm pair showed less drastic differences in their clearance and accumulation (Figure 4d), consistent with results obtained in single color imaging (Figure 3b and 3c). These results suggest that appropriately selected spectral signatures may allow reliable and high throughput screening of nanoparticle formulations for tumor-targeting using multispectral imaging.

Recent studies have debated over the impact of specific nanoparticle formulations, for example the attachment of antigen-specific targeting ligands, on their tumor targeting efficiency.[29] Interpreting existing results has been quite challenging because the choice of particle formulation and tumor model simultaneously affects multiple pharmacokinetic parameters,[30] and because *ex vivo* sampling only captures a snapshot of the tumor localization dynamics. Multispectral imaging may be useful in this regard.

3. Conclusion

In conclusion, we have systematically elucidated parameters controlling nanoparticle-fluorophore interactions, which may lead to novel strategies for developing in vivo fluorescent probes for imaging and delivery applications. Using this information, we demonstrated that an array of fluorescent-labeled GNPs could be fabricated for multicolor imaging of whole-animal tumor xenografts. For GNPs that are currently being developed as injectable therapeutics and carriers against cancer,[31] preclinical fluorescence imaging could be utilized to track their in vivo fate as part of the test to ensure efficacy and safe of use.

Supporting Information

Supporting Information is available from the Wiley Online Library or from the author.

Acknowledgements

We would like to acknowledge the Canadian Institute of Health Research and Canadian Breast Cancer Research Alliance (MOP - 193110 and RMF111623), Natural Sciences and Engineering Research Council (RGPIN 288231-09 and BIOPSYS Network), Canadian Foundation for Innovation, Ontario Centre of Excellence, and Ministry of Research and Innovation for funding support. L.C. would like to acknowledge Natural Sciences and Engineering Research Council for support for graduate studies.

Received: March 19, 2012
Published online: August 20, 2012

[1] a) E. Boisselier, D. Astruc, *Chem Soc Rev* **2009**, *38*, 1759; b) M. A. Dobrovolskaia, S. E. Mcneil, *Nat Nanotechnol* **2007**, *2*, 469; c) A. Albanese, P.S.Tang, W.C.W.Chan, *AnnRevBiomedEng* **2012**, *14*, 1.

[2] a) K. Donaldson, D. Brown, A. Clouter, R. Duffin, W. MacNee, L. Renwick, L. Tran, V. Stone, *J Aerosol Med* **2002**, *15*, 213; b) T. S. Hauck, A. A. Ghazani, W. C. W. Chan, *Small* **2008**, *4*, 153; c) N. Gou, A. Onnis-Hayden, A. Z. Gu, *Environ Sci Technol* **2010**, *44*, 5964; d) H. C. Fischer, L. C. Liu, K. S. Pang, W. C. W. Chan, *Adv Funct Mater* **2006**, *16*, 1299; e) R. H. Yang, L. W. Chang, J. P. Wu, M. H. Tsai, H. J. Wang, Y. C. Kuo, T. K. Yeh, C. S. Yang, P. Lin, *Environ Health Persp* **2007**, *115*, 1339; f) A. M. Derfus, W. C. W. Chan, S. N. Bhatia, *Nano Lett* **2004**, *4*, 11.

[3] a) A. E. Nel, L. Madler, D. Velegol, T. Xia, E. M. V. Hoek, P. Somasundaran, F. Klaessig, V. Castranova, M. Thompson, *Nat Mater* **2009**, *8*, 543; b) M. Lundqvist, J. Stigler, G. Elia, I. Lynch,

T. Cedervall, K. A. Dawson, *P Natl Acad Sci USA* **2008**, *105*, 14265; c) C. D Walkey, J. B. Olsen,H.Guo, A. Emili, W. C. W. Chan, *JAm Chem Soc* **2012**, *134*, 2139; d) A. Verma, F. Stellacci, *Small* **2010**, *6*, 12.

[4] K. L. Aillon, Y. M. Xie, N. El-Gendy, C. J. Berkland, M. L. Forrest, *Adv Drug Deliver Rev* **2009**, *61*, 457.

[5] a) N. Khlebtsov, L. Dykman, *Chem Soc Rev* **2011**, *40*, 1647; b) H. C. Fischer, W. C. W. Chan, *Curr Opin Biotech* **2007**, *18*, 565.

[6] a) S. D. Perrault, C. Walkey, T. Jennings, H. C. Fischer, W. C. W. Chan, *Nano Lett* **2009**, *9*, 1909; b) R. A. Petros, J. M. DeSimone, *Nat Rev Drug Discov* **2010**, *9*, 615; c) G. D. Zhang, Z. Yang, W. Lu, R. Zhang, Q. Huang, M. Tian, L. Li, D. Liang, C. Li, *Biomaterials* **2009**, *30*, 1928.

[7] a) S. D. Perrault, W. C. W. Chan, *Proc Natl Acad Sci USA* **2010**, *107*, 11194; b) H. S. Choi, W. H. Liu, F. B. Liu, K. Nasr, P. Misra, M. G. Bawendi, J. V. Frangioni, *Nat Nanotechnol* **2010**, *5*, 42.

[8] a) M. M. van Schooneveld, E. Vucic, R. Koole, Y. Zhou, J. Stocks, D. P. Cormode, C. Y. Tang, R. E. Gordon, K. Nicolay, A. Meijerink, Z. A. Fayad, W. J. M. Mulder, *Nano Lett* **2008**, *8*, 2517; b) N. Chanda, V. Kattumuri, R. Shukla, A. Zambre, K. Katti, A. Upendran, R. R. Kulkarni, P. Kan, G. M. Fent, S. W. Casteel, C. J. Smith, E. Boote, J. D. Robertson, C. Cutler, J. R. Lever, K. V. Katti, R. Kannan, *P Natl Acad Sci USA* **2010**, *107*, 8760; c) J. C. Sung, D. J. Padilla, L. Garcia-Contreras, J. L. VerBerkmoes, D. Durbin, C. A. Peloquin, K. J. Elbert, A. J. Hickey, D. A. Edwards, *Pharmaceut Res* **2009**, *26*, 1847.

[9] a) T. Schluep, J. Hwang, I. J. Hildebrandt, J. Czernin, C. H. J. Choi, C. A. Alabi, B. C. Mack, M. E. Davis, *P Natl Acad Sci USA* **2009**, *106*, 11394; b) A. M. Neubauer, H. Sim, P. M. Winter, S. D. Caruthers, T. A. Williams, J. D. Robertson, D. Sept, G. M. Lanza, S. A. Wickline, *Magn Reson Med* **2008**, *60*, 1353.

[10] J. Condeelis, R. Weissleder, *Csh Perspect Biol* **2010**, *2*.

[11] S. Gross, D. Piwnica-Worms, *Curr Opin Chem Biol* **2006**, *10*, 334.

[12] a) O. M. Bakr, B. H. Wunsch, F. Stellacci, *Chem Mater* **2006**, *18*, 3297; b) X. H. Huang, S. Neretina, M. A. El-Sayed, *Adv Mater* **2009**, *21*, 4880; c) S. D. Perrault, W. C. W. Chan, *J Am Chem Soc* **2009**, *131*, 17042; d) S. E. Skrabalak, J. Y. Chen, Y. G. Sun, X. M. Lu, L. Au, C. M. Cobley, Y. N. Xia, *Accounts Chem Res* **2008**, *41*, 1587; e) J. P. Xie, Q. B. Zhang, J. Y. Lee, D. I. C. Wang, *Acs Nano* **2008**, *2*, 2473.

[13] a) T. Lund, M. F. Callaghan, P. Williams, M. Turmaine, C. Bachmann, T. Rademacher, I. M. Roitt, R. Bayford, *Biomaterials* **2011**, *32*, 9776; b) J. M. Bergen, H. A. Von Recum, T. T. Goodman, A. P. Massey, S. H. Pun, *Macromol Biosci* **2006**, *6*, 506.

[14] a) P. Anger, P. Bharadwaj, L. Novotny, *Phys Rev Lett* **2006**, *96*; b) P. Bharadwaj, L. Novotny, *Opt Express* **2007**, *15*, 14266; c) Y. Chen, K. Munechika, D. S. Ginger, *Nano Lett* **2007**, *7*, 690; d) E. Dulkeith, A. C. Morteani, T. Niedereichholz, T. A. Klar, J. Feldmann, S. A. Levi, F. C. J. M. van Veggel, D. N. Reinhoudt, M. Moller, D. I. Gittins, *Phys Rev Lett* **2002**, *89*; e) M. Swierczewska, S. Lee, X. Y. Chen, *Phys Chem Chem Phys* **2011**, *13*, 9929; f) M. P. Singh, G. F. Strouse, *J Am Chem Soc* **2010**, *132*, 9383; g) T. Nakamura, S. Hayashi, *Jpn J Appl Phys 1* **2005**, *44*, 6833.

[15] G. Frens, *Nature-Physical Science* **1973**, *241*, 20.

[16] a) J. Satulovsky, M. A. Carignano, I. Szleifer, *P Natl Acad Sci USA* **2000**, *97*, 9037; b) I. Szleifer, J. Satulovsky, *Abstr Pap Am Chem S* **1999**, *218*, U477; c) G. F. Paciotti, L. Myer, D. Weinreich, D. Goia, N. Pavel, R. E. McLaughlin, L. Tamarkin, *Drug Deliv* **2004**, *11*, 169; d) T. Niidome, M. Yamagata, Y. Okamoto, Y. Akiyama, H. Takahashi, T. Kawano, Y. Katayama, Y. Niidome, *J Control Release* **2006**, *114*, 343.

[17] S. A. Hilderbrand, R. Weissleder, *Curr Opin Chem Biol* **2010**, *14*, 71.

[18] J. R. Lakowicz, *Anal Biochem* **2005**, *337*, 171.

[19] R. Wilson, D. V. Nicolau, *Angew Chem Int Ed* **2011**, *50*, 2151.

[20] G. Schneider, G. Decher, N. Nerambourg, R. Praho, M. H. V. Werts, M. Blanchard-Desce, *Nano Lett* **2006**, *6*, 530.

[21] a) M. Wang, M. Thanou, *Pharmacol Res* **2010**, *62*, 90; b) V. C. F. Mosqueira, P. Legrand, J. L. Morgat, M. Vert, E. Mysiakine, R. Gref, J. P. Devissaguet, G. Barratt, *Pharmaceut Res* **2001**, *18*, 1411.

[22] P. Kingshott, H. Thissen, H. J. Griesser, *Biomaterials* **2002**, *23*, 2043.

[23] a) B. Shi, C. Fang, Y. Y. Pei, *J Pharm Sci-Us* **2006**, *95*, 1873; b) C. Fang, B. Shi, Y. Y. Pei, M. H. Hong, J. Wu, H. Z. Chen, *Eur J Pharm Sci* **2006**, *27*, 27.

[24] a) R. K. Jain, T. Stylianopoulos, *Nat Rev Clin Oncol* **2010**, *7*, 653; b) M. E. Davis, Z. Chen, D. M. Shin, *Nat Rev Drug Discov* **2008**, *7*, 771.

[25] G. Alexandrakis, E. B. Brown, R. T. Tong, T. D. McKee, R. B. Campbell, Y. Boucher, R. K. Jain, *Nat Med* **2004**, *10*, 203.

[26] V. P. Chauhan, T. Stylianopoulos, Y. Boucher, R. K. Jain, *Annu Rev Chem Biomol* **2011**, *2*, 281.

[27] A. M. Herneth, S. Guccione, M. Bednarski, *Eur J Radiol* **2003**, *45*, 208.

[28] a) H. Lyng, O. Haraldseth, E. K. Rofstad, *Magn Reson Med* **2000**, *43*, 828; b) M. D. Pickles, P. Gibbs, M. Lowry, L. W. Turnbull, *Magn Reson Imaging* **2006**, *24*, 843.

[29] a) X. H. Huang, X. H. Peng, Y. Q. Wang, Y. X. Wang, D. M. Shin, M. A. El-Sayed, S. M. Nie, *Acs Nano* **2010**, *4*, 5887; b) C. H. J. Choi, C. A. Alabi, P. Webster, M. E. Davis, *P Natl Acad Sci USA* **2010**, *107*, 1235; c) K. F. Pirollo, E. H. Chang, *Trends Biotechnol* **2008**, *26*, 552.

[30] a) Y. H. Bae, K. Park, *J Control Release* **2011**, *153*, 198; b) A. Annapragada, K. B. Ghaghada, C. T. Badea, L. Karumbaiah, N. Fettig, R. V. Bellamkonda, G. A. Johnson, *Academic Radiology* **2011**, *18*, 20; c) R. K. Jain, S. K. Hobbs, W. L. Monsky, F. Yuan, W. G. Roberts, L. Griffith, V. P. Torchilin, *P Natl Acad Sci USA* **1998**, *95*, 4607.

[31] a) S. Lal, S. E. Clare, N. J. Halas, *Accounts Chem Res* **2008**, *41*, 1842; b) L. Tamarkin, S. K. Libutti, G. F. Paciotti, A. A. Byrnes, H. R. Alexander, W. E. Gannon, M. Walker, G. D. Seidel, N. Yuldasheva, *Clin Cancer Res* **2010**, *16*, 6139; c) J. F. Hainfeld, F. A. Dilmanian, D. N. Slatkin, H. M. Smilowitz, *J Pharm. Pharmacol.* **2008**, *60*, 977.